SNOM Imaging of a Crypt-Like Feature in Adenocarcinoma Associated with Barrett's Oesophagus

Timothy Craig, Andrew D. Smith, Gareth M. Holder, James Ingham, Caroline I. Smith, Andrea Varro, D. Mark Pritchard, Steve D. Barrett, David S. Martin, Paul Harrison, Andrzej Wolski, Antonio Cricenti, Marco Luce, Mark Surman, Swapan Chattopadhyay, Peter Weightman, and Michele R. F. Siggel-King*

The development of more accurate and sensitive diagnostic techniques is a key factor in efforts to improve cancer survival rates. The technique of infrared aperture fibre scanning near-field optical microscopy (IR-SNOM), together with radiation from the infrared free-electron laser (IR-FEL) on ALICE at Daresbury Laboratory (UK), has been used to obtain IR images of a crypt-like feature and the surrounding tissue; the tissue was taken from a patient with oesophageal adenocarcinoma and with a history of Barrett's oesophagus. We have shown that the DNA signal is enhanced relative to other contributions in the region of the crypt, and the glycoprotein signal shows a less pronounced increase in the region of the crypt. The Amide II signal is found to be anti-correlated with the DNA and glycoprotein profiles. The absorbance of the Amide II signal is found to differ for three different types of cancer tissue. High-resolution IR images of the crypt reveal additional structure that would not be resolved in diffraction-limited techniques.

1. Introduction

Cancer survival rates have steadily increased over the past few decades. Today, 50% of people who were diagnosed with cancer will live for 10 years or more whereas 40 years ago it was only 24%. There is a large variation in survival between cancer types. For example, prostate cancer has a 10-year survival rate of 84% whereas the corresponding prognosis for oesophageal cancer is much poorer with only 12%.[1] Oesophageal cancer shows the fastest rise in incidence of cancer in the Western world and although survival rates are improving, progress on this cancer lags behind that of many other cancers.[2,3]

Oesophageal adenocarcinoma often develops from a precursor condition known as Barrett's oesophagus, which is caused by acid reflux from the stomach whereby the acid damages the lower part of the oesophagus. Patients with Barrett's oesophagus have periodic surveillance endoscopies in which small sections of tissue (biopsies) are removed, subjected to Haematoxylin and Eosin (H&E) staining, then examined with an optical microscope in order to assess for the presence of premalignant dysplasia. Typically, the interobserver discordance for the diagnosis of the low-grade dysplasia characteristic of the onset of disease is greater than 50%.[4] Although this discordance

Dr. T. Craig, Dr. A. D. Smith[†], Dr. G. M. Holder, J. Ingham,
Dr. C. I. Smith, Dr. S. D. Barrett, Dr. D. S. Martin, P. Harrison,
Prof. A. Wolski, Prof. S. Chattopadhyay[‡,§], Prof. P. Weightman,
Dr. M. R. F. Siggel-King
Department of Physics, University of Liverpool
Liverpool L69 7ZE, UK
E-mail: michele.siggel-king@stfc.ac.uk

Prof. A. Varro, Prof. D. M. Pritchard
Department of Cellular and Molecular Physiology
Institute of Translational Medicine, University of Liverpool
Liverpool L69 3GE, UK

The ORCID identification number(s) for the author(s) of this article
can be found under https://doi.org/10.1002/pssb.201700518.

Dr. A. D. Smith, Prof. A. Wolski, Dr. M. Surman,
Prof. S. Chattopadhyay, Dr. M. R. F. Siggel-King
Cockcroft Institute
Sci-Tech Daresbury, Warrington WA4 4AD, UK

Dr. A. Cricenti, M. Luce
Istituto di Struttura della Materia, CNR
via del Fosso del Cavaliere 100, 00133 Rome, Italy

Dr. A. D. Smith, Dr. M. Surman, Dr. M. R. F. Siggel-King
Accelerator Science and Technology Centre (ASTeC)
STFC Daresbury Laboratory
Sci-Tech Daresbury, Warrington WA4 4AD, UK

[†]Present address: Dalton Cumbrian Facility, University of Manchester,
Westlakes Science and Technology Park, Cumbria CA24 3HA, UK
[‡]Present address: Department of Physics, Northern Illinois University,
DeKalb, IL 60115, USA
[§]Present address: Fermi National Accelerator Laboratory, Fermilab, PO
Box 500, Batavia, IL 60510-5011, USA

is reduced to ≈15% for the diagnosis of the more serious condition of high-grade dysplasia, there is a need to improve the accuracy of diagnosis since false positives can give rise to unnecessary procedures and false negatives can be fatal.[4] There is thus a need to improve the accuracy of diagnosis so that the disease can be treated before it has metastasised to other organs. In Barrett's oesophagus, the tissue in the distal oesophagus becomes more like the tissue in the lining of the intestine, a histological feature called intestinal metaplasia. One of the changes that occurs is that crypts,[5] which are absent in normal healthy squamous epithelial oesophageal tissue, develop in the oesophagus. As in most cancers, the origin of the cancer has remained elusive, though Barker et al.[5] have proposed that crypts are the origin of intestinal cancer.

Vibrational infrared spectroscopy provides a unique finger-print for molecules. Wang et al.[4] used Fourier transform infrared (FTIR) spectroscopy to characterise endogenous biomolecules in Barrett's oesophagus. This study showed that DNA, protein, glycogen and glycoprotein comprise the principal sources of infrared absorption in the 5.6–10.5 μm (1800–950 cm^{-1}) regime but lacked the spatial resolution to link the biomolecules to specific moieties within the tissue. Quaroni and Casson[6] used confocal IR microscopy and synchrotron radiation to study Barrett's oesophagus and oesophageal adenocarcinoma. Crypt features were present in their samples and the results showed that the Barrett's tissue had characteristic regions localised to gland crypts that displayed IR spectra with defined absorption features characteristic of glycoproteins. However, this study lacked the spatial resolution to specifically characterise these features and to detect them in the cancerous tissue.

Considerable progress has been made by applying FTIR spectral imaging to the examination of cancerous tissue[7–11] and this approach has considerable potential to improve the accuracy of cancer diagnosis. However, the spatial resolution that can be obtained with FTIR is limited by diffraction and the strength of the technique derives from the capability to record images at several thousand wavelengths simultaneously. Recently, the technique of infrared aperture fibre scanning near-field optical microscopy (IR-SNOM)[12] has been used to image cancerous tissue and cells. This technique is not limited by diffraction and it can yield images with high spatial resolution though time constrains limit its application to a small number of wavelengths. In this work, tissue from the lower oesophagus of a patient with a history of Barrett's oesophagus and with oesophageal adenocarcinoma has been imaged using IR-SNOM.

2. Experimental Section

The experiments were carried out using the infrared free-electron laser (IR-FEL) on the ALICE energy recovery linear accelerator at Daresbury.[13,14] Superconducting accelerator technology was utilised in ALICE to deliver 60 pC electron bunches at 16.25 MHz within long pulse trains of up to 100 μs at 10 Hz. The intense pulses of IR light are generated in an oscillator FEL,[13,14] which is quickly and easily tuneable through the mid-IR range by changing the undulator gap. Additional

range can be achieved by varying the electron energy in the accelerator. In this work the energy of the beam in the FEL was 27.5 MeV. A schematic of the layout is shown in **Figure 1**. The FEL beam is transported to the experimental area in an evacuated beamline. The ultra-high vacuum of the ALICE accelerator is separated from the lower vacuum of the beamline by a diamond window. In the experimental room, the FEL beam is split using a CaF$_2$ beam-splitter located in an evacuated optics box (B7 in Figure 1). Approximately 80% of the beam was sent to the experiment and 20% of the beam was sent through an Acton SP2500 spectrometer for diagnostics. The split beams exit the beamline (just after M10 in Figure 1) and optics box through CaF$_2$ windows and then travel through air.

The FEL power was measured using single element pyro-electric detectors. At the exit of the FEL, in the accelerator hall (PD1 in Figure 1), the average power was typically 10 mW. In the experimental room, just after M10 at the end of the evacuated beamline (PD3 in Figure 1), the average power was measured to be ≈1 mW. The dramatic reduction of FEL power through the beamline was due to two factors. The first was that one of the mirrors, M3, which was a toroidal mirror, was overfilled, resulting in a reduction of both power and beam quality.[15,16] The second was due to the large number of optics required to transport the beam from the accelerator hall to the experimental area, which is usual in such facilities.

The wavelength of the FEL was set by altering the gap of the undulator. At the beginning of the experimental run, a calibration curve was established by measuring the wavelength of the FEL beam, using the spectrometer, as a function of undulator gap setting. The near-linear relationship was used to establish a look-up table that was used for the duration of the run. The tuning range of the FEL was ≈λ = 6–9 μm (1700–1100 cm^{-1}). These measurements also enabled the determination of the bandpass as a function of wavelength. The typical spectral resolution of the FEL for this study was measured to be 0.13 μm (≈20 cm^{-1}) FWHM at λ = 8 μm. This resolution is adequate to resolve the distribution of significant spectral resonances.[17]

The SNOM employed in this work was built by the Rome group specifically for use at Daresbury. It was very similar to the one described previously.[17] The main difference is that it had an extended scanning range to enable imaging areas of ≈400 × 400 μm^2; the previous SNOM was limited to images of ≈40 × 40 μm^2. A photograph of the SNOM at the time of data collection for this work is shown in **Figure 2**. The SNOM is secured to a laser table. The tissue, which is on a small round slide, is attached to the base of the SNOM. A camera allows positioning of the sample and assists during the engaging of the tip. The inset in the upper left corner shows a view of a sample through this camera. The end of the fibre tip can be seen coming down from the centre of the top of this image. Although the tip appears large, there is a small part that protrudes that is not visible in this image. SNOM image spatial resolutions of ≈0.1 μm are achievable. For reference, the small red square, which has been superimposed onto the tissue sample in the camera image, is ≈40 × 40 μm^2. During data acquisition a Perspex shielding box surrounded the SNOM to reduce noise. The operation of an aperture fibre SNOM has been described in detail.[12] In brief, in the set-up used for this work, the sample
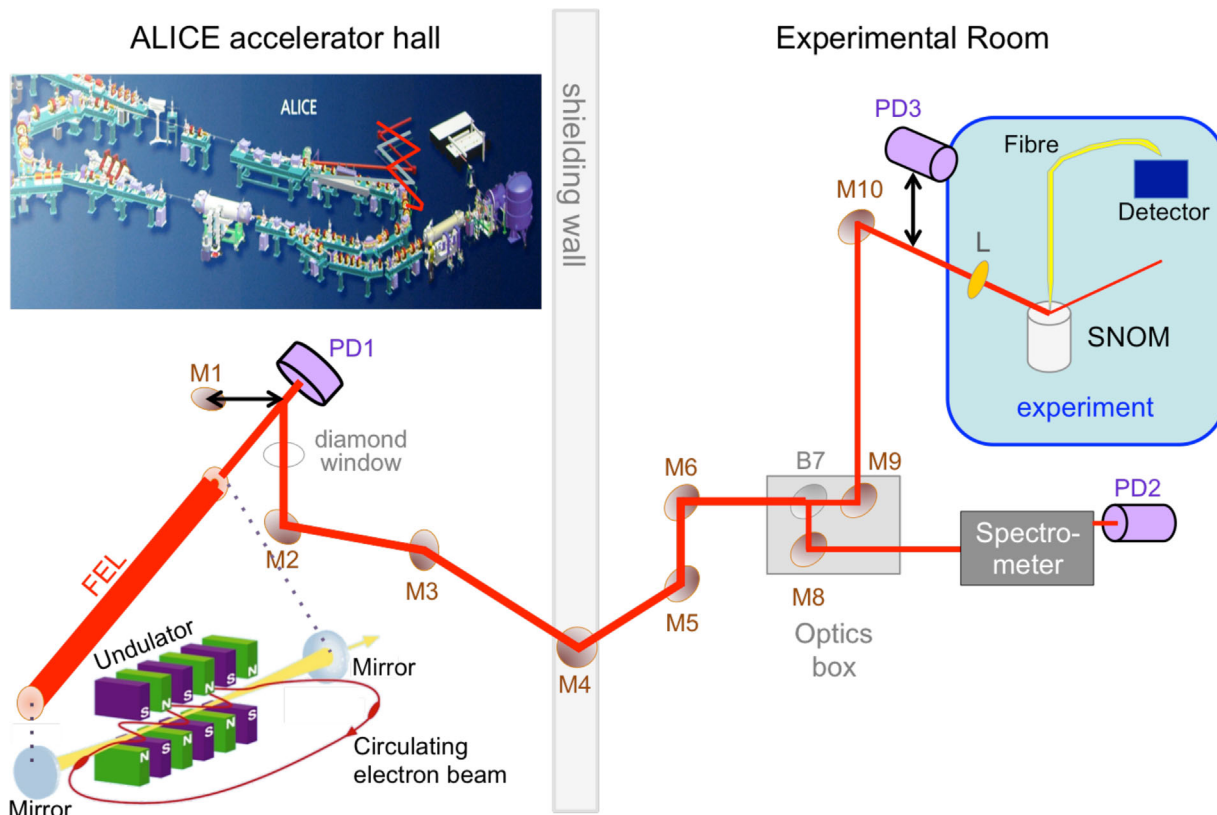
Figure 1. Schematic of the layout of the ALICE FEL beamline and experimental end-station. The following designations have been used: M# = mirror, B# = CaF$_2$ beam splitter, L = lens, PD = pyroelectric detector.
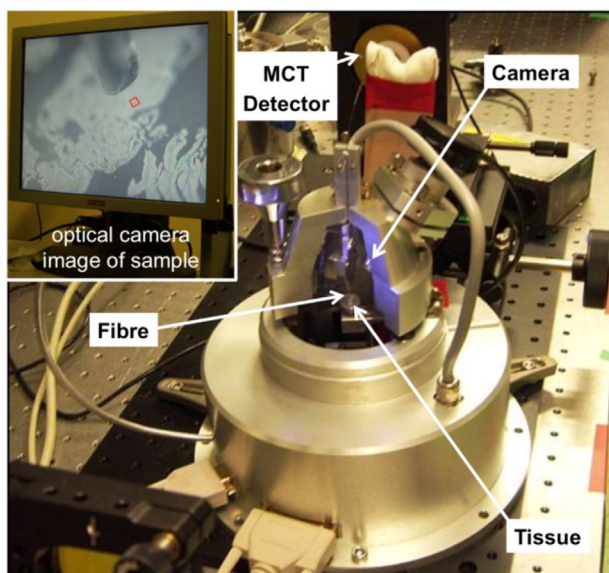
Figure 2. Photograph of the SNOM. The slide containing the tissue was mounted on the moving piezo-controlled platform. A microscope camera enables the sample to be viewed (inset in upper left corner). The fibre, which is barely visible, collects the light from the sample and transports it to the MCT detector.

was mounted in the SNOM on a platform that moved in three orthogonal directions. The IR light was focused onto the sample at a grazing angle of ≈15° to the plane of the sample. A specially prepared fibre[18,19] collected the light that encountered its small diameter tip, which is sensitive to the non-diffracting evanescent wave radiating from the illuminated surface. During SNOM imaging the sample was rastered in the horizontal plane; the sample-to-tip distance was kept constant using shear-force feedback and moving the sample in the vertical dimension. The relative height of the platform was recorded to give a topographic image of the surface. The SNOM (or light) image was obtained by recording the amount of light collected by the tip at each pixel. The greater the absorption by the sample, the less light detected. The light collected by the fibre was transported to a highly sensitive liquid-nitrogen cooled mercury cadmium telluride (MCT) detector. Images were collected at fixed wavelengths of the IR light. The relative intensity of the monochromatised beam at the exit of the spectrometer (PD2 in Figure 1) was measured and recorded concomitantly with the SNOM and topographic signals.

Following appropriate ethical committee approval and informed patient consent, oesophageal biopsy samples were obtained using standard biopsy forceps from patients attending for diagnostic oesophago-gastro-duodenoscopy at Royal Liverpool and Broadgreen University Hospitals NHS Trust. Biopsies were obtained from patients with Barrett's associated oesophageal adenocarcinoma. These were fixed in 10% formalin and

embedded in paraffin wax. Histological diagnosis was confirmed by a Consultant Gastrointestinal Histpathologist using the standard H&E staining technique as part of routine patient care. A series of $5\,\mu m$ sections from the paraffin block were subsequently cut using a microtome, then mounted onto $10\,mm$ diameter CaF_2 slides. Shortly before being imaged with the SNOM, the tissue was dewaxed using xylene. Optical images of the slide that was used for this study are shown in **Figure 3**b–d. One of the $5\,\mu m$ sections was subjected to H&E staining.

The H&E-stained image (Figure 3a) was used to identify a suitable region, which contained a variety of tissue types, including a crypt-like feature. The chosen area was located within the tissue on the CaF_2 slide using an optical microscope. The slide was then transferred to the SNOM where an incorporated optical microscope camera (see Figure 2), was used to approximately position the tissue under the tip. The sample was finely positioned by obtaining topographic images until the desired position was achieved.

IR-SNOM image sets comprising a topographic image, an IR image and a relative intensity reference image were collected over the crypt feature in the oesophageal cancer specimen. Large-scale images of nominal size $340 \times 340\,\mu m^2$ with 170×170 pixels were collected at $\lambda = 6.50$, 7.30, 8.05 and $8.60\,\mu m$. These wavelengths were chosen because they are biomarkers for Amide II, protein, DNA and glycoprotein, respectively. A total of three image sets, all taken at $\lambda = 8.05\,\mu m$, were obtained throughout the experiment; these were used to establish reproducibility of the measurement and stability of the tissue. For higher resolution imaging, the raster scan step size setting was then reduced (2, 1, 0.5 and $0.25\,\mu m$) and images of successively smaller sizes were collected at $\lambda = 8.05\,\mu m$ whilst keeping the total number of pixels constant at 170×170. Following the acquisition of the image taken with a nominal step size of $0.25\,\mu m$ the tissue in the region of the crypt was destroyed by the scanning tip, preventing the acquisition of images at higher resolution.

All images were processed using Gwyddion software.[20] The $340\,\mu m$ topographic image was levelled by fitting a plane through three points. The SNOM images were corrected for beam dropouts by manually selecting the affected pixels and then interpolating using the nearby pixels. A Gaussian filter was then applied to the SNOM images and the colour images enhanced using adaptive non-linear colour mapping.

3. SNOM Images of a Crypt-Like Feature in Cancerous Tissue

Optical images of the cancerous tissue imaged in this work are shown in Figure 3. The H&E-stained tissue was used to identify a suitable crypt-like feature for imaging (see Figure 3a). This crypt-like structure reflected the relatively well-differentiated nature of this particular oesophageal adenocarcinoma. Within the tissue there were also other areas of malignant epithelial cells, as well as stroma, that were not organised into crypt-like features. The crypt-like feature is located in the central biopsy on the CaF_2 slide (Figure 3b). An optical microscope image of this area is shown in Figure 3c with an enlarged section shown in Figure 3d, where the crypt-like feature can be clearly seen. The red squares in Figure 3c and d show the approximate area of the stained image in Figure 3a. Figure 3a and d are very similar but are not exactly the same because they are from different $5\,\mu m$ sections of the wax plug containing the biopsies. However, since they were taken in close proximity to each other the tissue is not expected to change significantly over the small distances involved and the stained image can be used to identify tissue types in the SNOM images.

The topographic and IR images taken at $\lambda = 8.05\,\mu m$ are shown in **Figure 4** for the four image sets taken at different step sizes. Each individual image was colour mapped between highest and lowest values to emphasise the additional detail that is resolved as the resolution of the image increases. Although each image was taken with an equal step size setting in both the x- and y-dimensions, and with 170×170 pixels, the actual step sizes varied for each setting due to non-linearities in the piezo drives. The smaller-scale images have each been size corrected by matching the topographies of each smaller-scale image to the next larger-scale image. In general, little or no correction was applied to the size of the y-dimension of the pixel. The x-dimension, however, decreased with increasing resolution. This resulted in the smaller-scale images being rectangular in shape and of dimensions $142 \times 167\,\mu m^2$, $62 \times 83.5\,\mu m^2$ and
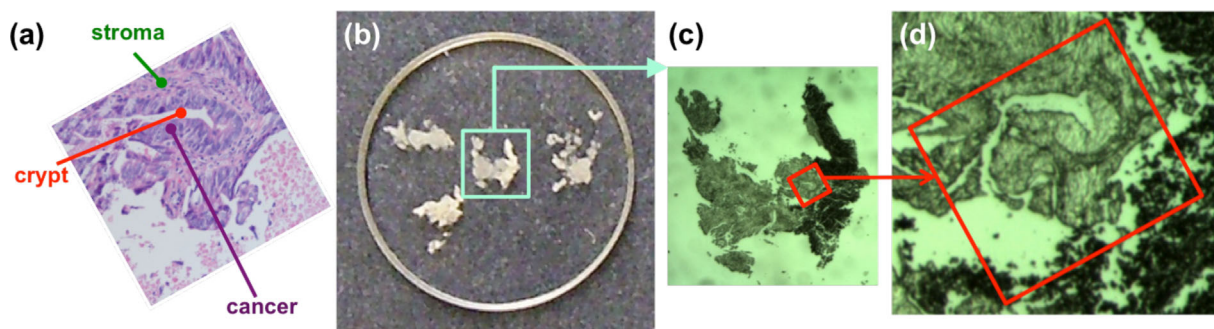
Figure 3. Optical images of cancerous tissue. a) Optical microscope image of the H&E-stained area containing the crypt-like feature. b) Photograph of $10\,mm$ diameter CaF_2 slide containing four biopsies from the same patient taken at the same time. c) Optical microscope image of dewaxed tissue. d) Optical microscope image of dewaxed tissue showing details of the crypt-like feature. The largest area scanned by the SNOM is shown by the red squares in (c) and (d).
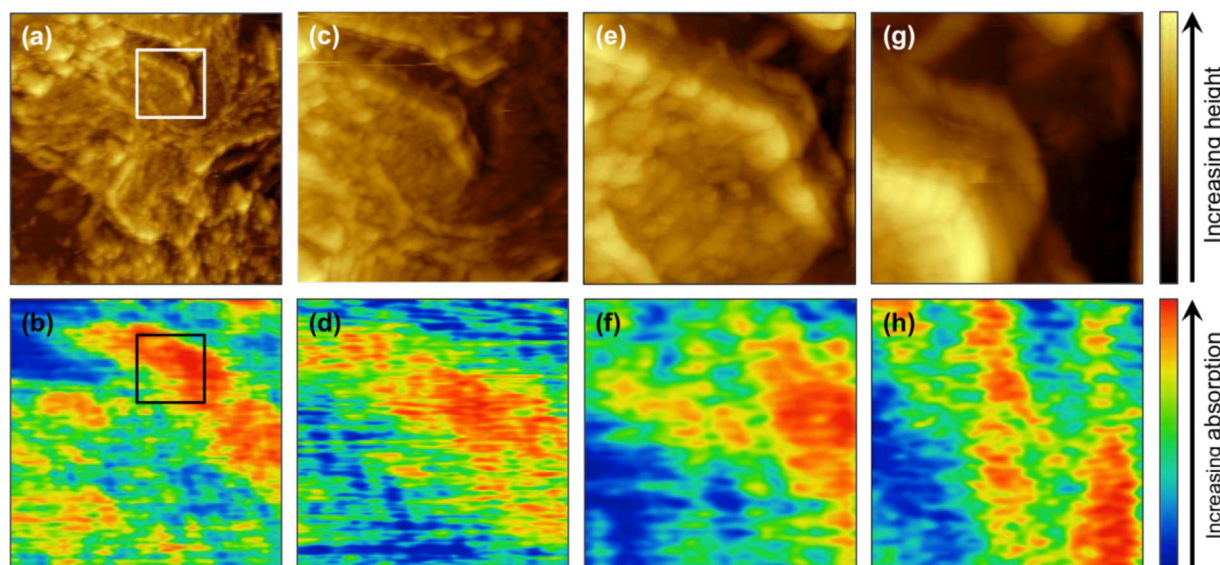
Figure 4. Topography (top) and IR (bottom) images of the crypt-like feature taken at $\lambda = 8.05\,\mu m$. a and b) Image size is $334 \times 334\,\mu m^2$ with a pixel size of $2\,\mu m$. c and d) Image size is $142 \times 167\,\mu m^2$. e and f) Image size is $62 \times 83.5\,\mu m^2$. g and h) Image size is $31.5 \times 42\,\mu m^2$. The overlaid squares on (a) and (b) show the approximate location of the zoomed images in (e) and (f). The colours of each image have been scaled independently to reveal the features within each image.

$31.5 \times 42\,\mu m^2$ relative to the large-scale image of nominal size of $334 \times 334\,\mu m^2$.

The crypt-like feature can be clearly seen around the region of the superimposed white square at the top of the image in Figure 4a. Three independent scans of this region were obtained at $\lambda = 8.05\,\mu m$ to ensure reproducibility; one of these is shown in Figure 4b. The black square in Figure 4b is at the same relative location as the white square in Figure 4a. The most intense areas of absorption are shown by the red colours. In Figure 4b these areas are concentrated at the location of the crypt, whereas the rest of the tissue absorbs at a lower intensity. Clearly the crypt-like feature is associated with an enhancement of the $\lambda = 8.05\,\mu m$ biomarker for DNA relative to this region of the adenocarcinoma.
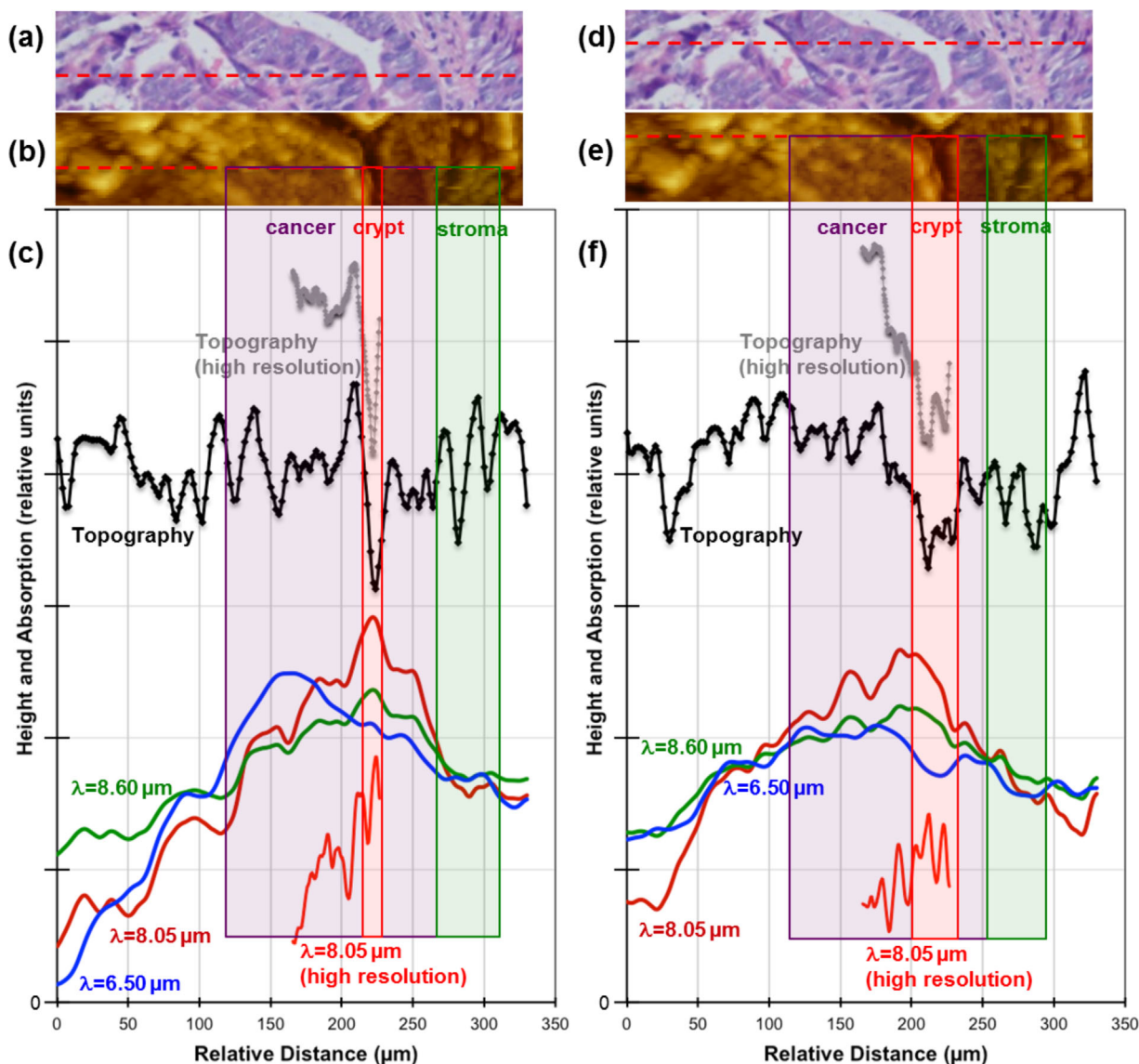
The region of the crypt-like feature was further explored by zooming onto it with increasing spatial resolution (Figure 4c–h). The white and black squares in Figure 4a and b show the approximate locations of the images in Figure 4e and f. As the resolution of the images is increased, more detailed features become resolved. From the IR images in Figure 4b, d, f and h, it can be seen that the highest absorption at $\lambda = 8.05\,\mu m$ occurs inside the crypt and along its edges; this is indicative of the region with the largest concentration of DNA.

To gain a better perspective on the behaviour of different types of tissue within the sample, **Figure 5** shows line profiles across the images at two locations within the tissue. Figure 5b and e show the line in the topography image from which the IR profiles were taken; its profile is shown as a black line with symbols in Figure 5c; the symbols are located at the centre of each pixel. As can be seen, the line passes through the crypt-like feature near the minimum in its topography and in Figure 5e the line passes through one of the widest parts of the crypt. In Figure 5b and c, the deepest part of the crypt occurs at a distance

of $\approx 223\,\mu m$. Figure 5a and d shows the stained image with lines added at the approximate positions from which the profiles were taken. Since the stained tissue image and the topographic image are not from the same slice of tissue there are small differences between them but this does not prevent the stained images being used to identify the different types of tissue within the sample. The stained images were used as a guide to identify areas on each profile representing the crypt-like feature, other areas within the cancerous tissue and stroma; these are shown in Figure 5c and f as shaded rectangles. Figure 5c and f show the absorption profiles of different wavelengths of light along the two horizontal lines through the largest-scale tissue image. The line profiles for the large-scale IR images, taken at $\lambda = 8.05$, 8.60 and $6.50\,\mu m$ are shown as solid overlapping lines. The two shorter lines in each figure are from one of the higher resolution scans taken at $\lambda = 8.05\,\mu m$.

In both positions, the line profiles for $\lambda = 8.05\,\mu m$ (DNA) and $\lambda = 8.60\,\mu m$ (glycoprotein) are similar in shape. There is, however, an important difference between the two profiles. The $\lambda = 8.05\,\mu m$ line shows a relatively large increase over the region of the crypt-like feature compared with its intensity over the rest of the image; the $\lambda = 8.60\,\mu m$ line is relatively flat and shows only a small increase at the crypt. These results are consistent with the findings of Quaroni[6] who imaged a crypt in Barrett's tissue – in the region of the crypt, the DNA intensity was enhanced relative to the glycoprotein signal. In non-dysplastic Barrett's oesophagus tissue the crypts are expected to be the source of new cells,[6] however, it is not clear how this could relate to the crypt-like feature that we have observed.

The profiles for $\lambda = 6.50\,\mu m$ (Amide II) are, to some extent, anti-correlated with the profiles for $\lambda = 8.05\,\mu m$ and $\lambda = 8.60\,\mu m$. The $\lambda = 6.50\,\mu m$ profile shows maximum absorption in the region to the left of, and adjacent to the crypt-like feature. Cancer

ADVANCED
SCIENCE NEWS

www.advancedsciencenews.com

p s s
physica status solidi b

www.pss-b.com

Figure 5. Line profiles of two locations through the crypt-like feature: (a) and (d) sections of the stained image with the dashed red line showing the approximate location of the profiles, (b) and (e) sections of the topography image with the dashed red line showing the location of the profiles, and (c) and (f) the line profiles. The shaded rectangles identify areas on each profile representing the crypt-like feature, cancerous tissue and stroma.

is a complex mixture of different types of cells. This can be seen in the stained image (Figure 5a and d) which shows at least three general types of cancerous tissue: the crypt, the dark purple striated region and the pink and lighter purple pattern. Just as these three different types of tissue exhibit different stained image patterns, they also exhibit differing levels of Amide II.

The two shorter curves in Figure 5c and f were taken with a smaller step size and show additional details of the structure of the profile in the region of the crypt-like feature. In both lines, the DNA profiles show maxima in the deepest part of the crypt. In Figure 5f, these maxima occur on the edges of the crypt. The IR images have been spatially filtered, which results in a loss of resolution and hence a continuity of signal across the crypt.

These curves illustrate the potential of the aperture fibre IR-SNOM technique to resolve features below the diffraction limit.

4. Conclusions

Using an aperture fibre IR-SNOM, we have obtained high-resolution images in the region of a crypt-like feature in tissue taken from a patient with adenocarcinoma and with a history of Barrett's oesophagus. The DNA signal was found to be enhanced relative to other contributions in the region of this crypt-like feature and a less pronounced increase in the glycoprotein signal was observed in the same region. Finally, the Amide II signal was

found to be anti-correlated with DNA and glycoprotein profiles and its absorbance was found to differ for three different areas within this cancerous tissue.

Conflict of Interest

The authors declare no conflict of interest.

[1] Cancer Research UK, http://www.cancerresearchuk.org/health-professional/cancer-statistics/survival.

[2] B. K. Edwards, E. Ward, B. A. Kohler, C. Eheman, A. G. Zauber, R. N. Anderson, A. Jemal, M. J. Schymura, I. Lansdorp-Vogelaar, L. C. Seeff, M. van Ballegooijen, S. L. Goede, L. A. G. Ries, *Cancer* **2010**, *116*, 544.

[3] B. A. Kohler, E. Ward, B. J. McCarthy, M. J. Schymura, L. A. Ries, C. Eheman, A. Jemal, R. N. Anderson, U. A. Ajani, B. K. Edwards, *J. Natl. Cancer Inst.* **2011**, *103*, 714.

[4] T. D. Wang, G. Triadafilopoulos, J. M. Crawford, L. R. Dixon, T. Bhandari, P. Sahbaie, S. Friedland, R. Soetikno, C. H. Contag, *Proc. Natl. Acad. Sci. USA* **2007**, *104*, 15864.

[5] N. Barker, R. A. Ridgway, J. H. van Es, M. van de Wetering, H. Begthel, M. van den Born, E. Danenberg, A. R. Clarke, O. J. Sansom, H. Clevers, *Nature* **2009**, *457*, 608.

[6] L. Quaroni, A. G. Casson, *Analyst* **2009**, *134*, 1240.

[7] A. S. Haka, K. E. Shafer-Peltier, M. Fitzmaurice, J. Crowe, R. R. Dasari, M. S. Feld, *Proc. Natl. Acad. Sci. USA* **2005**, *102*, 12371.

[8] B. R. Smith, K. M. Ashton, A. Brodbelt, T. Dawson, M. D. Jenkinson, N. T. Hunt, D. S. Palmer, M. J. Baker, *Analyst* **2016**, *141*, 3668.

[9] K. Gajjar, J. Trevisan, G. Owens, P. J. Keating, N. J. Woods, H. F. Stringfellow, P. L. Martin-Hirsch, F. L. Martin, *Analyst* **2013**, *138*, 3917.

[10] H. Chen, Z. Lin, L. Mo, T. Wu, C. Tan, *BioMed Res. Int.* **2015**, *2015*, 472197.

[11] P. Bassan, J. Mellor, J. Shapiro, K. Williams, M. Lisanti, P. Gardner, *Anal. Chem.* **2014**, *86*, 1648.

[12] A. Cricenti, R. Generosi, M. Luce, P. Perfetti, G. Margaritondo, D. Talley, J. S. Sanghera, I. D. Aggarwal, N. H. Tolk, *Phys. Chem. Chem. Phys.* **2002**, *4*, 2738.

[13] D. J. Dunning, N. R. Thompson, J. A. Clarke, I. Burrows, D. M. P. Holland, S. Leonard, Int. Free Electron Laser Conf. — FEL 2009 (Eds: S. Waller, V. R. W. Schaa, M. Marx, L. Liljeby, J. Poole, H. Owen), Liverpool, UK, August **2009**, pp. 583–586.

[14] N. R. Thompson, D. J. Dunning, J. A. Clarke, M. Surman, A. D. Smith, Y. Saveliev, S. Leonard, *Nucl. Instrum. Methods Phys. Res. A* **2012**, *680*, 117.

[15] After the experimental run on which this data was collected, ALICE and the FEL beamline were upgraded, including a new, larger toroidal mirror. Typical average power at PD1 is now 15 mW and at PD3 it is ∼10 mW.

[16] N. R. Thompson, J. A. Clarke, T. Craig, D. J. Dunning, O. V. Kolosov, A. Moss, Y. M. Saveliev, M. R. F. Siggel-King, M. Surman, P. D. Tovee, P. Weightman, Int. Free Electron Laser Conf. — FEL 2015 (Eds: H. S. Kang, D.-E. Kim, V. R. W. Schaa), Daejeon, Korea, August **2015**, pp. 379–383.

[17] A. D. Smith, M. R. F. Siggel-King, G. M. Holder, A. Cricenti, M. Luce, P. Harrison, D. S. Martin, M. Surman, T. Craig, S. D. Barrett, A. Wolski, D. J. Dunning, N. R. Thompson, Y. Saveliev, D. M. Pritchard, A. Varro, S. Chattopadhyay, P. Weightman, *Appl. Phys. Lett.* **2013**, *102*, 053701.

[18] D. T. Schaafsma, R. Mossadegh, J. S. Sanghera, I. D. Aggarwal, J. M. Gilligan, N. H. Tolk, M. Luce, R. Generosi, A. Cricenti, P. Perfetti, G. Margaritondo, *Ultramicroscopy* **1999**, *77*, 77.

[19] D. B. Talley, L. B. Shaw, J. S. Sanghera, I. D. Aggarwal, A. Cricenti, R. Generosi, M. Luce, G. Margaritondo, J. M. Gilligan, N. H. Tolk, *Mater. Lett.* **2000**, *42*, 339.

[20] D. Nečas, P. Klapetek, *Cent. Eur. J. Phys.* **2012**, *10*, 181. http://gwyddion.net/.